LBL--28172

DE90 008666

Invited paper to be published in the *Proceedings of the Symposium on Exotic Nuclear Spectroscopy, Division of Nuclear Chemistry and Technology, American Chemical Society, Miami Beach, Florida, September 11-15, 1989*, edited by Wm. C. McHarris, Plenum Publishing.

NUCLEAR DECAY STUDIES FAR-FROM-STABILITY

R.B. Firestone, J.M. Nitschke, P.A. Wilmarth, K.S. Vierinen[a], R.M. Chasteler, J. Gilat[b], A.A. Shihab-Eldin[c]

Lawrence Berkeley Laboratory,
Berkeley, CA 94730
December 4, 1989

[a]Permanent address: University of Helsinki, SF00180, Finland.
[b]Permanent address: Soreq Nuclear Research Center, Yavne 70600, Israel.
[c]Permanent address: Kuwait Institute for Scientific Research, Kuwait.

1. INTRODUCTION

Nuclear decay studies far-from-stability are performed not merely to characterize new isotopes, but to establish an experimental footing for improving our theoretical understanding of nuclear structure and decay. Although progress has been made in explaining low-lying level structure for a broad range of nuclei, transition probabilities are not yet quantitatively understood. The ability to understand nuclei far-from-stability is important to astrophysics for extending r- and s-process calculations to unknown nuclei, and to nuclear engineering for decay-heat calculations. Mass formulas are particularly sensitive to the known Q-values for nuclei far-from-stability. Finally, by studying nuclei far-from-stability, we probe extremes of both decay energy and proton-neutron ratios where unforseen and important new nuclear properties may be exhibited. To understand these nuclei it is important that complete decay information be determined without resorting to nuclear models which will bias the interpretation of the results.

The decays of nearly 100 isotopes and isomers have been studied with the OASIS mass-separation facility on-line at the Lawrence Berkeley Laboratory SuperHILAC. These studies have concentrated on neutron-deficient nuclei with $55 \le Z \le 71$ up to $A=157$ and neutron-rich nuclei with $166 \le A \le 174$. An extensive detector array has been constructed to detect x-rays, γ rays, protons, alpha particles, betas, and their coincidences either beta- or particle-delayed or directly emitted by ground-state or isomeric decay. From these data fairly complete decay schemes have been constructed for many isotopes, and decay Q-values and EC/β^+ ratios have been determined. Analysis techniques have been developed to infer the electron-capture intensities from x-ray data, positron intensities from 511-keV annihilation intensities, internal conversion coefficients from coincidence data, and spins from beta-delayed proton final-state feedings.

The results of these experiments are combined in this paper with those from many other laboratories to provide insight into systematic trends of beta- and γ-ray transition probabilities near N=82. It is hoped that the smooth systematic trends in these transition probabilities will provide clues towards interpreting the underlying nuclear structure. Nuclei near N=82 and Z=64 are expected to be spherical and should be described by simple Shell Model considerations. Away from the shell closures, deformation sets in which should exhibit itself in the transition probabilities. The Z=64 shell closure is expected to disappear near N=78. The qualitative nature of these phenomena will be discussed.

2. SOURCE PREPARATION

Most nuclides investigated at OASIS[1] were produced by bombarding various targets with heavy-ion beams of up to 8.5 MeV/u from the Berkeley SuperHILAC. The reactions and beam energies were chosen on the basis of compound nuclear reaction cross sections calculated with the ALICE [2] evaporation code. Targets were mounted near the high temperature surface ionization source of the OASIS on-line mass separator facility in a configuration optimized for low transverse velocity recoils from compound nucleus reactions. The ion source is efficient for all isotopes between Cs and Lu, however elements outside that region had ionization potentials that were too high to allow them to be observed. Mass resolution of about one part in 800 was used, and no impurities from adjacent mass chains have been observed. After mass separation of the evaporation residues, a beam of the radioactive reaction products was deflected by an electrostatic mirror to a shielded spectroscopy laboratory ~4 m above the mass separator. There, the activity was deposited on a programmable moving tape which positioned it, in a user selectable time cycle, in the center of an array of β, γ and charged particle detectors. Sources could be transported from the collection to detection points in 70 ms and tape cycles as short as 1.28 s have been used. The ALICE calculations could not be tested quantitatively due to uncertainties in the ionization efficiency and the diffusion time, however the results appear to qualitatively agree with the predictions in most cases. A diagram of the OASIS mass separator is given in fig. 1.

Neutron-excess nuclei were produced by multinucleon transfer reactions. Here the targets are located inside the high temperature region of the ion source and are restricted to refractory materials like W or Ta. To overcome this restriction, heavy-ion rare-earth beams were used to produce projectile-like neutron-rich rare-earth isotopes. In these experiments natural tungsten targets were bombarded with 8.5 MeV/u ^{170}Er and ^{176}Yb ions to produce isotopes of Dy, Ho, Er, and Tm. Low cross-sections, expected for the desired product nuclei, were partially offset by the scarcity and relatively long-half lives of the reaction impurities within an isobaric chain. A principal source of contamination came from Lu isotopes produced

in these reactions.

3. DETECTORS

The detector array used for these measurements has evolved significantly since the first OASIS measurements were begun. The present detector geometry is shown in fig. 1. A Si ΔE-E particle telescope and a hyperpure Ge (HPGe) face the front (deposit) side of the the collection tape. The telescope records proton and alpha events and identifies betas which are stopped in the HPGe detector. The HPGe detector also is used to measure x-rays and low-energy γ rays. A 1-mm thick plastic scintillator and a 52% n-type Ge detector faces the opposite side of the tape. The scintillator allows the vetoing of betas which would otherwise be recorded in the 52% Ge spectrum. A 24% n-type Ge detector, oriented at 90° to the other two, was placed ~4.5 cm from the radioactive source. This detector was less subject to the summing of coincident γ rays than the 52% Ge detector and was used to analyze the γ-ray singles intensities.

The singles spectra in the HPGe and 52% Ge detectors were recorded in multispectrum mode with the tape cycle divided into eight equal time intervals. These spectra were used to determine precise half-lives and to establish the genetic relationships between parent and daughter species. Coincidences and timing information between the various detectors were recorded event-by-event and monitored by on-line sorting with preselected gates; all coincidence events were tagged with a time signal relative to the beginning of a tape cycle for half-life information.

4. DATA ANALYSIS TECHNIQUES

4.1. DECAY SCHEME NORMALIZATION

In order to determine the emission probabilities of γ rays and to infer the beta feedings, it is necessary to determine the total electron capture and positron decay branching intensities. When the ground state is not directly fed by beta decay, the normalization factor necessary to convert relative transition intensities to intensity per decay is the sum of transition intensities feeding the ground state and long-lived excited states plus the branching intensities for other modes of decay (e.g. alpha, β-delayed proton, and IT modes). The statistical methods required to correctly calculate this normalization were discussed by Browne [3,4] and Firestone [5]. If the decay scheme is not well known, and substantial, unobserved transition intensity might populate the ground state, this method is unreliable.

Another method for determining the normalization is to follow the genetic relationship of parents and daughters. If the daughter activity is much shorter lived than the parent, equilibrium will occur, and if the normalization of either species is determined, the other normalization can be directly calculated. It is important to remember that at equilibrium the daughter activity R_d is greater than the parent activity R_p and related to the parent and daughter half-lives by the equation

$$R_d = R_p \frac{t_{1/2}(p) - t_{1/2}(d)}{t_{1/2}(p)} \qquad (1)$$

When equilibrium is not possible the relative parent/daughter normalizations can be determined by following the growth and decay.

In the OASIS studies, it was often possible to determine the decay scheme normalization from the measured electron capture and positron decay intensities. The methods used to investigate these intensities are discussed below.

4.1.1. ELECTRON CAPTURE INTENSITY

A signature of electron capture decay is K x-ray emission. For the nuclei discussed here, the resolution of the HPGe detector was sufficient to resolve the $K\alpha_{1,2}$ and $K\beta_{1,2}$ x-rays of adjacent elements. This analysis

was performed using a modified version of the SAMPO code [6]. The relative x-ray intensities for each element are well known [7], and our measured intensity ratios normally agreed well with the expected values. Table 1 shows a representative comparison of our measured values with the known branchings. To determine the relative intensity of electron capture, the K x-ray intensities were corrected for contributions from internal conversion, although in some cases internal conversion was negligible and could be ignored. Otherwise, the K-conversion coefficients must be estimated and a correction applied. Often, this correction was large with respect to the electron capture intensity and the electron capture feeding could not be reliably determined. If the positron feeding were known (Sec. 4.1.2) it was sometimes possible to estimate the electron capture branching intensity from the decay scheme and expected EC/β^+ ratios. After the K x-ray intensity associated with electron capture was determined, additional corrections for fluorescence yield [8] and $I_{EC(K)}/I_{EC(tot)}$ [9] were applied.

4.1.2. POSITRON INTENSITY

A signature of positron decay is the emission of 511-keV annihilation radiation symbolized by $\gamma^{\pm}$. In most experiments several positron emitters were produced simultaneously. Distinction between the various positron emitters could only be made on the basis of half-life and was particularly difficult when complex relationships between parent and daughter activities occurred. To solve this problem, a multilinear analysis method was developed. The key to this method was to follow the decay of a prominent γ ray associated with each positron-emitting isotope. The relative $\gamma^{\pm}$ intensity associated with each γ ray is constant at all times. Thus, the total observed $\gamma^{\pm}$ intensity in any spectrum from i positron-emitting species is given by

$$I_{\gamma}^{\pm}(tot) = C_{\gamma}^{\pm}(1)I_{\gamma}(1) + C_{\gamma}^{\pm}(2)I_{\gamma}(2) + \ldots + C_{\gamma}^{\pm}(i)I_{\gamma}(i) \qquad (2)$$

where $C_{\gamma}^{\pm}(i)$ is the proportionality constant relating the γ-ray intensity to the annihilation intensity associated with that decay. An advantage of this method is that data taken at various dwell times with differing reactions could be analyzed simultaneously. The calculation was performed using the computer code BANAL [10] with the IMSL multilinear analysis subroutine RLMUL [11]. An example calculation is shown in table 2.

The resulting $\gamma^{\pm}$ intensity for each isotope must be corrected for annihilation-in-flight [12] and source geometry. These corrections were not entirely straightforward because a 4π positron annihilator was not used. The correction factor was determined by comparison of results using this method with other techniques discussed above, and with β-delayed proton data where the positron and electron capture intensities in coincidence with protons must equal the total proton intensity. The uncertainty in this correction was estimated as 10% by comparison with results obtained by the equilibrium method. This comparison for A=142 nuclei is shown in Table 3. The multilinear analysis method described here can also be used to resolve γ-ray multiplets and unusually complex x-ray spectra.

4.2. Q_{EC} DETERMINATION

Two methods have been employed in these experiments to determine Q_{EC} values. The EC/β^+ ratio for the decay to a level can be inferred from the K x-ray and $\gamma^{\pm}$ intensities in coincidence with transitions deexciting that level. If the level is not significantly populated from above and the deexciting transition is not in coincidence with a K x-rays from internal conversion, then this method is straightforward. For the 4.7-MeV level in ^{149}Ho, populated by ^{149}Er^m decay, coincidence data for the intense 4.7-MeV γ ray gives EC/β^+=0.68±0.34 which corresponds to Q_{EC}=$9.1^{+0.9}_{-0.4}$. The excitation energy of ^{149}Er^m is 0.74 MeV, so for the ^{149}Er ground-state Q_{EC}=$8.4^{+0.9}_{-0.4}$. Similarly, ^{149}Er^g populates four narrow resonances in ^{149}Ho which decay by β-delayed proton emission. From the ratio of intensities in the proton singles and positron-coincident proton spectra, (EC+β^+)/β^+ can be determined. The value of (Q_{EC}-B_p) can be determined by minimizing the differences between the experimental and theoretical values as a function of Q_{EC}. The result of this minimization for ^{149}Er is shown in fig. 2 where (Q_{EC}-B_p)=$7.0^{+0.5}_{-0.4}$ was determined. Wapstra *et*

al. [13] report a systematic proton binding energy B_p=1.2±0.2 which gives Q_{EC}=8.2±0.5 in good agreement with the value from the 4.7-MeV level analysis.

A second method for determining Q_{EC} was to vary the decay energy so that the measured electron capture and positron decay branching intensities [see 4.1.1 and 4.1.2] matched those predicted from the established decay scheme. This method is most effective when the decay scheme is well known. Decays in the A=140 and A=142 mass chains are particularly suited to this method because their decays are dominated by intense ground-state β-feedings. These high-energy, low log*ft* transitions are so dominant that missing higher level feedings are not expected to be significant for all but the most neutron-deficient isotopes. A summary of these results is given in Table 4 where they are compared with the evaluated values of Wapstra *et al.* [14], and the calculated values of Liran and Zeldes [15]. Agreement is excellent, particularly for the previously known values, lending confidence to this method.

4.3. INTERNAL CONVERSION COEFFICIENTS

Internal conversion data are necessary to determine the spins and parities of levels populated in these decays. Unfortunately, conversion electrons were not measured at OASIS so other methods have been employed to obtain some internal conversion information. One method was to determine the K-conversion coefficient from the ratio of K x-ray to γ-ray intensities in coincidence with transitions feeding a level. Another method was to utilize the intensity balance in singles or coincidence data to infer total conversion coefficients. For example, these methods were used to determine the multipolarities of transitions following $^{142}Tb^{m}$ IT decay. This decay scheme is shown in fig. 3 and the coincidence spectra gating on the 182- and 212-keV transitions are shown in fig. 4. From the 212-keV gate we determined that α_K(68.5)=61±5 which is consistent with the theoretical α_K(M2)=64 [16]. From the relative intensities of the 29.7-, 68.5-keV γ-ray transitions and the Tb K x-rays in the 182-keV gate we determined that α_{tot}(29.7)=44±15 which is consistent with the multipolarity M1+(6±3)%E2. A summary of the conversion coefficients determined in these experiments is given in Table 5.

4.4. SPIN VALUES FROM FINAL STATE β-DELAYED PROTON FEEDINGS

The spins of isotopes decaying by β-delayed proton emission are reflected in the distribution of final-state feedings to the proton decay daughter. Unlike alpha-particle decay where the formation of the alpha in the nucleus is complex, proton decay is a simple process which is well understood. Thus, if the beta-strength distribution associated with the decay to the region of proton emission is known or the decay can be treated within the framework of a statistical model, the final-state feedings can be calculated and compared with experiment. A detailed discussion of this method for spin assignment has been discussed by Wilmarth[17]. The experimental final-state feedings were determined from pγ-coincidence information where the ground-state feeding was determined by the difference in the coincidence proton intensity and the total proton intensity. Results of this method for odd-A precursors are shown in Table 6, and a comparison of results using various β-strength models for ^{153}Yb decay is given in Table 7.

5. SUMMARY OF NUCLEI STUDIED WITH OASIS

The nuclei studied with OASIS have been summarized in Table 8. It is not possible to discuss all of the decay schemes which were investigated in this paper so only a few decays of particular nuclear structure interest will be discussed below.

5.1. N=81 NUCLEI

The decay of nuclei with N=81 and Z≥64 is characterized by hindered β-transitions to low-lying levels in the N=82 daughter and strong transitions to levels above 4 MeV. These nuclei can be understood in terms

of the shell model where the single neutron vacancy in the $\nu s_{1/2}$ orbital cannot be filled by decaying protons in $\pi d_{5/2}$ or $\pi g_{7/2}$ orbitals. Only by exciting neutron pairs can orbitals be made available for beta decay. The decay of ^{145}Gd(1/2+) has been explained[18] with a weak coupling model. In this model, single-particle proton states in the daughter are assumed to to act as spectators only weakly interacting with the core excitations. For ^{145}Gd decay, two levels near the 2^+ and two levels near the 4^+ ^{144}Sm core excitations dominate. Above 4 MeV, however, about 12.8% of the beta intensity was observed[19] despite a Q_{EC}=5.07 MeV. The log*ft*=4.3 to this region is similar to that of nearby $\pi h_{11/2} \rightarrow \nu h_{9/2}$ spin-flip transitions. This strong transition presumably populates 3-quasiparticle levels with the structure $(\pi h_{11/2})(\nu h_{9/2})(\nu s_{1/2})$.

Similar decay systematics have been observed for decay of the $1/2^+$ and $11/2^-$ isomer pairs in ^{147}Dy[20,21], ^{149}Er[22], and ^{151}Yb[23,24]. Remarkably, the spin-flip decays of the isomer pairs are nearly identical, confirming the weak-coupling assumption that the odd $\nu s_{1/2}$ or $\nu h_{11/2}$ neutron is a spectator. A comparison of the log*ft* values for the dominant configurations contributing to the N=81 decays is given in Table 9. The odd-odd decays display similar decay patterns further confirming the weak-coupling assumptions.

The spectator neutrons become important when the 3-quasiparticle configurations deexcite to the ground configurations. The $\nu h_{9/2}$ neutron can decay by a fast M1 spin-flip to fill the $\nu h_{11/2}$ vacancy, an analogous transition to the beta decay, but is very hindered filling the $\nu s_{1/2}$ vacancy. This affect has been observed in several ways. In ^{145}Gd($1/2^+$) decay, the 3-quasiparticle levels deexcite preferentially to levels above 1.7 MeV. Transitions to low-lying single-particle states are weak and both M1 and E2 transitions are of comparable intensity. For 3 MeV transitions, this corresponds to a factor of 60 greater hindrance for M1 transitions. In ^{149}Er[$11/2^-$] decay, the 3-quasiparticle levels deexcite primarily by M1 spin-flip transitions to the $\nu h_{11/2}$ ground state and by weaker E1 transitions to the $\nu g_{7/2}$ level. No evidence for low-energy γ-ray transitions is observed. Additional evidence is obtained from β-delayed proton data. The proton spectrum from ^{149}Er^{g+m} decay is shown in fig. 5. The structured part of the spectrum is known to belong to the low-spin decay, and the 7(2)% branching intensity is much larger than the 0.4% predicted from Gross Theory[25,26]. Similarly, the low-spin β-delayed proton branching intensity for ^{147}Dy decay is enhanced by a factor of 20 and Schardt et al[27] have measured the very weak γ-rays deexciting the levels corresponding to the structured part of the proton spectrum. The γ-ray transitions appear to be hindered, enhancing the proton intensity. The nature of this hindrance has been discussed by Nitschke *et al.*[28]

5.2. ONSET OF DEFORMATION AT Z=64

Unlike the Z=50 and N=82 shells, the Z=64 subshell gap is small, about 1.8 MeV, compared to the ~4.5 MeV gap observed at N=82. The Z=64 subshell rapidly disappears as we move off of the N=82 shell closure. Above Z=64 we observe the emergence of nearly degenerate $\pi s_{1/2}$ and $\pi h_{11/2}$ isomeric states in odd-Z even-N nuclei. For odd-A Tb isotopes this pattern holds for $80 \le N \le 86$. At N=78, Redon *et al.*[29] have established a $5/2^+$ ground state, and no evidence exists for the β-decay of the $11/2^-$ isomer. In fig. 6 the decay scheme for ^{141}Tb, measured at OASIS, is presented. The decay data support a $5/2^-$ spin assignment for ^{141}Tb. Möller[30] has performed a Nilsson/QRPA calculation of the excited states in ^{141}Tb which is presented in fig. 7. For deformations in the ε_2=0.1-0.2 range, the $5/2^-$[532] orbital is predicted for the ground state in agreement with experiment. The ^{143}Tb ground-state spin is less obvious from the QRPA calculation, however, the $5/2^+$[402] state increases rapidly with deformation and at ε_2~0.1 its energy is near to 4 or 5 other states and it may be the ground state.

6. SYSTEMATICS OF SHELL MODEL TRANSITIONS NEAR N=82

The available proton and neutron shell model states important for nuclei near N=82 are listed in figure 8. Single particle levels corresponding to these states are well known and observed at low excitations in the odd-A nuclei in this region. Additional levels occur in the odd-A nuclei near energies close to the energies

of the even-even core excitations (2^+, 3^-, 4^+, etc). The energetics of these nuclei can be explained, simply, by a weak-coupling model where the single-particle levels are combined with core levels to create the observed configurations. Residual interactions break the degeneracy of these configurations, creating the observed level scheme, up to at least 3 MeV.

The preceding arguments are qualitative in nature and appear to explain the level schemes for many nuclei near N=82. Transition probabilities for decays between levels in this region are a more rigorous test of a model. In the following discussions, the log*ft* and reduced γ-ray transition probabilities of nuclei in this region are explored.

6.1. LOG*FT* VALUES

Most transitions in the N=82 region have log*ft*>5. A few transitions are much faster and can dominate a particular decay scheme. Inspection of the shell model states in fig. 8 reveals two, important spin-flip transitions which may be expected. Below N=82, the $\pi d_{5/2} \rightarrow \nu d_{3/2}$ transition is important, and above Z=64 the $\pi h_{11/2} \rightarrow \nu h_{9/2}$ transition is significant. Evidence for both transitions is found in a series of $0^+ \rightarrow 1^+$ transitions. In these transitions either a $(\pi d_{5/2})^2$ or a $(\pi h_{11/2})^2$ pair can be assumed to decay by the spin-flip transition.

The experimental log*ft* values for these transitions are plotted in fig. 9. For N≤80, the transitions should involve the $\pi d_{5/2}$ protons, and for transitions with N≥82 the $\pi h_{11/2}$ protons are involved. In fig. 10 the prediction from the simple shell model for each transition is included for comparison. From the shell model,

$$ft_{S.M.} = \frac{6160}{g_a^2 B(GT)} \tag{3}$$

where g_a=1.263, $B(GT) = n\frac{4l}{2l+1}$, and n is the number of valence protons. The shell model predictions are nearly an order of magnitude faster than experiment, a phenomenon commented on previously by Nolte *et al.*[31] for the N=82 region and by Barden *et al.*[32] for the Z=50 region ($\pi g_{9/2} \rightarrow \nu g_{7/2}$ transitions). Towner[33] has argued that these discrepancies are due to pairing correlations, core polarization, and higher-order phenomena. Nevertheless, several curiosities remain to be explained.

The n dependence appears to be reproduced in the spin-flip transitions where the average log*ft* value changes between n=2 and n=6 by 0.47(9) for N=76,78 and N=82,84. This agrees closely with the shell model expectation of 0.48. The N=80 transitions have been excluded from the average because the shell model predicts that the $\nu d_{3/2}$ orbital is filled, blocking the spin-flip transition. This can be demonstrated by comparing the N=76 and N=78 log*ft* values. They differ, on average, by 0.22(12) which is consistent with 0.3 predicted if the $\nu d_{3/2}$ orbital were half-filled at N=78. It is remarkable that these shell model trends are preserved, although calculations by Towner[33] do indicate that the hindrance should be constant for l=5 orbitals.

Additional trends in the log*ft* values can be seen in fig. 9. A constant log*ft*=5.0 is consistent with all values where Z=60 or N=80. The $\nu s_{1/2}$ and $\nu d_{3/2}$ orbital are nearly degenerate in this region, perhaps explaining the residual β-strength at N=80. Another intriguing trend in fig. 9 is the low log*ft* values for ^{142,144}Dy. The valence protons in these isotopes should be $(\pi h_{11/2})^2$ yet the log*ft* follows the $\pi d_{5/2}$ spin-flip trend. It is possible that the measured values are somewhat low due to missed β-strength to levels near 2 MeV in the daughter where the $\nu h_{9/2}$ orbitals are expected. This transition has been observed in ^{146}Dy decay[34] with log*ft*=3.8(2), consistent with the heavier Dy decays. Assuming that this transition occurs with the same log*ft* in the lighter Dy isotopes, about 35% of the decay would populate that resonance in ^{142}Dy decay, effectively raising the log*ft* for the ground state transition to the value from ^{140}Gd decay. A ~7% affect would occur for ^{144}Dy decay which is not sufficient to bring the ground-state log*ft* to the value for ^{142}Gd.

Other spin-flip transitions have been observed in odd-Z decays. The measured log*ft* values for $\pi d_{5/2} \rightarrow \pi d_{3/2}$ are summarized in fig. 11, and the $\pi h_{11/2} \rightarrow \pi h_{9/2}$ transitions are summarized in fig. 12. These transitions are substantially more retarded than the even-even decays and show little *n* dependence. The calculations of Towner[33] support the disappearance of *n* dependence, predicting a rapidly decreasing hindrance with increasing *n*. The $1^+ \rightarrow 0^+$ decays are shown in fig. 13. They are similar to the nearby $0^+ \rightarrow 1^+$ transitions and their log*ft* values increase by 0.50(11) from *n*=1 to *n*=5, nearly the 0.70 value predicted by the shell model. These transitions are comparable with the $0^+ \rightarrow 1^+$ transitions because they are transitions between the identical levels. Finally, there is a sequence of $9^+ \rightarrow 8^+$ transitions in odd-odd nuclei with N≥83. The log*ft* systematics for these transitions are shown in fig. 14. These decays have been described as $(\pi h_{11/2})(\nu f_{7/2}) \rightarrow (\nu h_{9/2})(\nu f_{7/2})$ transitions. Their log*ft* values fall intermediate to the single-particle and even-even decays.

6.2. REDUCED GAMMA-RAY TRANSITION PROBABILITIES

Several families of reduced transition probabilities for single-particle shell model transitions have been studied for nuclei near N=82. The M4 Weisskopf-reduced transition probabilities for the $\nu h_{11/2} \rightarrow \nu d_{3/2}$ transition are given in fig. 15. The B(M4) values exceed the Weisskopf estimates and slowly decline with increasing proton number. The large strength is consistent with the near closure of the N=82 shell but inconsistent with the expected blocking of the $\nu d_{3/2}$ orbital at N=81. The near degeneracy of the $\nu s_{1/2}$ and $\nu d_{3/2}$ orbitals apparently contributes to the large quasiparticle strength in $\nu d_{3/2}$. At N=79 the B(M4) values are similar to those at N=81 and slightly exceed them for Z≥60. This probably reflects the opening of the $\nu d_{3/2}$ orbital which offsets the greater distance from the closed shell.

At Z=52, B(M4) increases rapidly which is consistent with the proximity to the Z=50 closed proton shell. The B(M4) strength decreases until at mid-shell, Z=66, a minimum is reached. A small sub-shell effect may be observed at Z=64. It is tempting to predict that the B(M4) values will increase for Z≥68. This effect appears to be observed at Z=68 where a small increase in B(M4) is observed.

The E3 Weisskopf-reduced transition probabilities for the $\pi h_{11/2} \rightarrow \pi d_{5/2}$ transition are shown in fig. 16. The B(E3) values increase rapidly near N=82 greatly exceeding the Weisskopf estimates. In addition, the B(E3) values decrease with increasing proton number. As protons are added, the $\pi d_{5/2}$ orbital is progressively filled, partially blocking the E3 transition. At Z=59 there are no protons occupying the $\pi d_{5/2}$ orbital (the odd proton is in the $\pi h_{11/2}$ orbital), while at Z=63 four protons block that orbital. The B(E3) should be proportional to the number of $\pi d_{5/2}$ vacancies and decrease by 0.33 from Z=59 to Z=63. At N=82, the experimental B(E3) values decrease by 0.37(6) in that interval. Also, at Z=65 B(E3) is nearly zero, consistent with complete blocking of the $\pi d_{5/2}$ orbital.

M2 Weisskopf-reduced transition probabilities for the $\pi h_{11/2} \rightarrow \pi g_{7/2}$ transitions are summarized in fig. 17. These transitions are significantly hindered, except for ^{133}La which is nearly a full Weisskopf unit. The hindrance is not surprising because, except for ^{133}La, the $\pi g_{7/2}$ orbital is fully blocked. The modest strength at Z=57 is consistent with the $\pi g_{7/2}$ orbital being 2/3 full.

A considerable success for the shell model near N=82 has been its ability to explain numerous yrast E2 transition energies and transition probabilities. Lawson[35] has shown that seniority *v* is a good quantum number and the decays between $(\pi h_{11/2})^n$ configurations give B(E2) values proportionate to $(\frac{6-n}{6-v})^2$. Several experiments[31,36-39] have confirmed the predictions which are summarized in table 10.

7. CONCLUSIONS

A considerable body of data for the neutron-deficient rare earth nuclei have been measured at OASIS and other facilities. Improved experimental techniques and methods of data analysis have increased the amount of useful information in this region. Smooth trends in the log*ft* data near N=82 and qualitative consistency

with the shell model for beta and gamma transitions give hope that a consistent, simple explanation of these phenomena may be obtained. Towner has shown that pairing effects and core polarization may explain the discrepancies with the shell model, however these affects are difficult to calculate. Conversely, Lawson has found success in explaining shell model transitions in several nuclei with very few parameters. Similar explanations of the beta transitions may be found by the correct parameterization of the problem. It is remarkable that while the absolute transition probabilities vary from shell model transitions, the $0^+ \rightarrow 1^+$ beta transitions, E3 γ-ray transitions, and N=82 even-Z E2 transitions all scale with proton number exactly as predicted in the shell model.

The need for more precise measurements and additional data is apparent. Complete decay scheme information, including beta and gamma strength measurements, absolute delayed-particle emission probabilities, mass measurements, and level lifetimes are important for understanding nuclear decay and improving our ability to predict unmeasured decay properties. In particular, the neutron-deficient rare-earth nuclei above Z=64 need more investigation because of the importance of the $\pi h_{11/2}$ orbital in fast spin-flip beta- and gamma-ray transitions. Additional data is also required for the neutron deficient nuclei with Z≥72 where virtually no beta-decay data studies have been done. These nuclei offer experimental difficulties because they cannot be easily obtained at most mass separators. The low log$f$=2.3 for Z=74, predicted by the shell model, suggests that this region will provide some of the fasted beta transitions observed at any mass.

8. ACKNOWLEDGEMENTS

This work was supported by the Director, Office of Energy Research, Division of Nuclear Physics of the Office of High Energy and Nuclear Physics of the U.S. Department of Energy under contract DE-AC03-76SF00098.

REFERENCES

1. J.M. Nitschke, Nucl. Instr. and Meth. **206**, 341 (1983).

2. W.G. Winn, H.H. Gutbrot, and M. Blann, Nucl. Phys. **A188**, 423 (1972); M. Blann and J Bisplinghoff, "Code ALICE/Livermore 1982", U.S. DOE Report UCID-19614 (1982).

3. E. Browne, Nucl. Instr. and Meth. Phys. Res. **A249**, 461 (1986).

4. E. Browne, Nucl. Instr. and Meth. Phys. Res. **A265**, 541 (1988).

5. R.B. Firestone. "Analysis of α-, β-, and γ-ray Emission Probabilities", LBL-27109; to be published in Nucl. Instr. and Meth. Phys. Res.

6. J.T. Routti and S.G. Prussin, Nucl. Instr. and Meth. **72**, 125 (1969).

7. "Table of Isotopes, 7th Edition", edited by C.M. Lederer and V.S. Shirley; E. Browne, J.M. Dairiki, and R.E. Doebler principal authors, (John Wiley & Sons, New York, 1978).

8. W. Bambynek, B. Crasemann, R.W. Fink, H. -U. Freund, H. Mark, C.D. Swift, R.E. Price, and P.V. Rao, Rev. Mod. Phys. **44**, 716 (1972).

9. N.B. Gove and M.J. Martin, At. Data Nucl. Data Tables **A10**, 205 (1971).

10. Computer code BANAL for multilinear analysis, R.B. Firestone, unpublished.

11. Least-squares multilinear analysis subroutine RLMUL, International Mathematical and Statistical Library (IMSL) Version 9.2.

12. G. Azuelos and J.E. Kitching, At. Data Nucl. Data Tables **17**, 103 (1976).

13. A.H. Wapstra and G. Audi, Nucl. Phys. **A432**, 140 (1985).

14. A.H. Wapstra, G. Audi, and R. Hoekstra, At. Data Nucl. Data Tables **39**, 281 (1988).

15. S. Liran and N. Zeldes, At. Data Nucl. Data Tables **17**, 431 (1976).

16. F. Rosel, H.M. Fries, K. Alder, and H.C. Paul, At. Data Nucl. Data Tables **21**, 91 (1978).

17. P.A. Wilmarth, Ph.D. Thesis, University of California, Berkeley, 1988, Lawrence Berkeley Laboratory Report 26101.

18. R.B. Firestone, R.C. Pardo, R.A. Warner, Wm. C. McHarris, and W.H. Kelly, Phys. Rev. **C25**, 527 (1982).

19. G.D. Alkhazov, A.A. Bykov, V.D. Wittmann, S. Yu. Orlov, and V.K. Tarasov, Phys. Lett. **157B**, 350 (1985).

20. G.D. Alkhazov, A.A. Bykov, V.D. Wittmann, V.E. Starodubsky, S. Yu. Orlov, V.N. Panteleyev, A.G. Polyakov, and V.K. Tarasov, Nucl. Phys. **A438**, 482 (1985).

21. D. Schardt, P.O. Larsson, R. Kirchner, O. Klepper, V.T. Koslowsky, E. Roeckl, K. Rykaczewski, K. Zuber, N. Roy, P. Kleinheinz, and J. Blomqvist, *Proceedings of the 6th International Conference on Atomic Masses and Fundamental Constants (AMCO7), Darmstadt-Seeheim, 1984*, edited by O. Klepper, p. 222.

22. R.B. Firestone, J.M. Nitschke, P.A. Wilmarth, K. Vierinen, J. Gilat, K.S. Toth, and Y.A. Akovali,

Phys. Rev. C39, 219 (1989).

23. K.S. Toth, Y.A. Ellis-Akovali, J.M. Nitschke, P.A. Wilmarth, P.K. Lemmertz, D.M. Moltz, and F.T. Avignone III, Phys. Let. **178B**, 150 (1986).

24. P. Kleinheinz, B. Rubio, M. Ogawa, M. Piiparinen, A. Plochocki, D. Schardt, R. Barden, O. Klepper, R. Kirchner, and E. Roeckl, Z. Phys. A323, 705 (1985).

25. K. Takahashi, M. Yamada, and T. Kondoh, At. Data Nucl. Data Tables 12, 101 (1973).

26. K. Takahashi, private communication (1988).

27. D. Schardt, R. Barden, R. Kirchner, O. Klepper, A. Plochocki, E. Roeckl, P. Kleinheinz, M. Piiparinen, B. Rubio, K. Zuber, C.F. Liang, P. Paris, A. Huck, G. Walter, G. Marguier, H. Gabelmann, and J. Blomqvist, "Proceedings of the Fifth International Conference on Nuclei Far From Stability, Rosseau Lake, Ontario, Canada", edited by I.S. Towner (AIP Conference Proceedings, New York, 1988), p 477.

28. J.M. Nitschke, P.A. Wilmarth, R.B. Firestone, P. Möller, K.S. Toth, and J. Gilat, Phys. Rev. Lett. 62, 2805 (1989).

29. N. Redon, T. Ollivier, R. Beraud, A. Charvet, R. Duffait, A. Emsallem, J. Honkanen, M. Meyer, J. Genevey, A. Gizon, and N. Idrissi, Z. Phys. A325, 127 (1986).

30. P. Möller, private communication; P. Möller and J.R. Nix, Nucl. Phys. A361, 117 (1981).

31. E. Nolte, G. Korschinek, and Ch. Setzensack, Z. Phys. A309, 33 (1982).

32. R. Barden, R. Kirchner, O. Klepper, A. Plochocki, G.-E. Rathke, E. Roeckl, K. Rykaczewski, D. Schardt, and J. Zylicz, Z. Phys. A329, 319 (1988).

33. I.S. Towner, Nucl. Phys. A444, 402 (1985).

34. K. Zuber, C.F. Liang, P.Paris, J. Styczen, J. Zuber, P. Kleinheinz, B. Rubio, G. de Angelis, H. Gabelmann, A. Huck, J. Blomqvist, and the ISOLDE collaboration, CERN, Z. Phys. A327, 357 (1987).

35. R.D. Lawson, Z. Phys. A303, 51 (1981).

36. P.J. Daly, P. Kleinheinz, R. Broda, A.M. Stefanini, S. Lunardi, H. Backe, L. Richter, R. Willwater, and F. Weik, Z. Phys. A288, 103 (1978).

37. H. Helppi, Y.H. Chung, P.J. Daly, S.R. Faber, A. Pakkanen, I. Ahmad, P. Chowdhury, Z.W. Grabowski, T.L. Khoo, R.D. Lawson, and J. Blomqvist, Phys. Lett. **115B**, 11 (1982).

38. E. Nolte, G. Colombo, S.Z. Gui, G. Korschinek, W. Scholl[illegible]meier, P. Kubik, S. Gustavsson, R. Geier, and H. Morinaga, Z. Phys. A306, 211 (1982).

39. J.H. McNeill, J. Blomqvist, A.A. Chishti, P.J. Daly, W. Gelletly, M.A.C. Hotchkis, M. Piiparinen, B.J. Varley, and P.J. Woods, Phys. Rev. Let. 63, 860 (1989).

Table 1. Comparison of experimental and theoretical K x-ray intensities

	K_{α_1}		K_{α_2}		$K_{\beta_1'}$		$K_{\beta_2'}$	
	Expt	Th	Expt	Th	Expt	Th	Expt	Th
Nd	100(2)	100	50(4)	54.9	24(8)	30.0		8.3
Pm	100.0(12)	100	53.6(8)	55.1	30.6(12)	30.1		8.4
Sm	100.0(13)	100	54.6(7)	55.2	31.0(3)	30.2	8.8(3)	8.6
Eu	100.0(10)	100	55.7(8)	55.4	30.9(6)	30.5	8.5(2)	8.7
Gd	100.0(11)	100	56.4(9)	55.6		30.8		8.9
Tb	100(3)	100	50(2)	55.8	34(4)	31.0	10(3)	8.9
Dy	100(2)	100	55.2(13)	56.0		31.2	10(2)	8.9
Ho	100(2)	100	56.6(17)	56.2	29(6)	31.5	8.7(9)	8.8

Table 2a. Multilinear analysis of A=142 $\gamma^{\pm}$ intensities using the equation $I_{\gamma}^{\pm}(tot) = C_{\gamma}^{\pm}(1)I_{\gamma}(1) + C_{\gamma}^{\pm}(2)I_{\gamma}(2) + \ldots + C_{\gamma}^{\pm}(i)I_{\gamma}(i)$.

Input Relative γ-ray Intensities $I_{\gamma}(i)$				Input $I\gamma^{\pm}$(tot)		Fitted $I\gamma^{\pm}$(tot)	
Eu(768)	Gd(179)	Tb(515)	Dy(182)	I(511)	ΔI(511)	I(511)	χ^2
426	100	678	0	6839	280	6830	0.001
531	100	56	7	5330	280	5482	0.298
60	100	0	0	944	90	958	0.024
1051	100	289	32	11476	574	11507	0.003
850	100	157	16	8835	442	8882	0.011
693	100	88	13	7342	367	7172	0.215
492	100	50	9.3	5230	262	5162	0.066
383	100	38	8.4	4148	207	4136	0.003
301	100	25	8.1	3356	168	3354	0.0001
251	100	21	6.3	2811	140	2859	0.120
201	100	19	3.4	2380	119	2347	0.075

Table 2b. Parameters $C_{\gamma}^{\pm}(i)$ calculated with the computer code BANAL

Isotope	Parameter	Lower-bound	Upper-bound	Std. Error
^{142}Eu	8.83	8.37	9.30	0.16
^{142}Gd	4.28	3.13	5.42	0.40
^{142}Tb	3.89	3.57	4.21	0.11
^{142}Dy	20.9	6.6	35.3	5.0

Table 3. Summary of decay branchings for A=142

Isotope	$t_{1/2}$[a]	Branching intensity			E_γ	I_γ[b]	I_γ[c]
		β^+	EC	Proton			
^{142}Pm	40.5(5) s	0.771(27)	0.229(27)		1576.1	0.0196(11)	
^{142}Sm	72.49(5) min	<0.05	>0.95				
^{142}Eu	2.34(12) s	0.899(16)	0.101(16)		768.0	0.102(7)	≡0.102(3)
^{142}Gd	70.2(6) s	0.48(5)	0.52(5)		178.9	0.112(12)	0.113(5)
^{142}Tb	597(17) ms	0.968(4)	0.032(4)	$2.4(10)\times10^{-5}$	515.3	0.249(17)	≡0.249(13)
^{142}Dy	2.3(3) s	0.90(4)	0.10(4)	$8(3)\times10^{-3}$	181.3	0.043(8)	0.51(5)

[a]Values for ^{142}Pm and ^{142}Sm are from L.K. Peker, Nucl. Data Sheets 43, 579 (1984). Other values from this work.
[b]Normalized to measured EC+β^+ intensity
[c]Equilibrium intensity normalized to indicated transitions

Table 4. Comparison of experimental and theoretical decay energies

	Q_{EC}(MeV)		
Isotope	Experiment	Wapstra el al[a]	Liran-Zeldes[b]
^{140}Eu	8.6(4)	8.4(5)	8.3
^{140}Gd	4.8(4)	4.5(7)	5.5
^{140}Tb	>11.3	10.7(11)	10.9
^{142}Pm	4.88(16)	4.87(4)	5.1
^{142}Sm	<2.1	2.10(4)	2.2
^{142}Eu	7.0(3)	7.40(10)	7.5
^{142}Gd	4.2(3)	4.2(4)	4.6
^{142}Tb	10.4(7)	10.0(7)	9.9
^{142}Dy	7.1(2)	6.4(11)	7.1
^{149}Er	8.4(5)	7.0(9)	8.65
	Q_{EC}-B_p (MeV)		
	Experiment	Wapstra et al[a]	Liran-Zeldes[b]
^{145}Dy	5.8(4)	5.9(7)	6.1
^{147}Dy	4.4(3)	4.5(1)	4.8
^{147}Er	8.4(3)	8.2(7)	8.6
^{148}Ho	5.7(5)	5.2(3)	5.9
^{149}Er	7.0(5)	5.8(9)	7.3
^{150}Tm	7.5(3)	7.6(7)	8.4
^{151}Yb	8.8(4)	8.9(9)	9.7
^{152}Lu	9.6(9)	10(1)	10.7
^{153}Yb	5.7(4)	6.1(5)	6.0

[a] A.H. Wapstra, G. Audi, and R. Hoekstra, At. Data Nucl. Data Tables 39, 281 (1988).

[b] S. Liran and N. Zeldes, At. Data Nucl. Data Tables 17, 431 (1976).

Table 5. Experimental and theoretical conversion coefficients from OASIS

Parent	E_γ	α_K(expt)	α_K(theory)[a] E1	E2	E3	M1	M2	M3	M4	Adopted Multipolarity
$^{140}Eu^m$	185.3	0.19(4)	0.046	0.19	0.70	0.28	1.55	6.83	29.5	E2
$^{142}Tb^m$	29.7	44(15)[b]	1.50	521	-	12.5	1130	-	-	M1+E2
	68.5	61(5)	0.68	2.48	5.93	5.69	63.8	278	911	M2
$^{144}Tb^m$	113.7	4.59(20)	0.18	0.81	3.00	1.32	10.1	51.0	241	E3+M4
		28(2)[b]	0.21	1.65	22.6	1.57	13.4	96.1	855	
^{145}Ho	66.3	6.5(10)	0.24	2.40	4.59	6.83	77.3	298	788	M1
$^{149}Er^{g+m}$	111.3	1.82(11)	0.20	0.82	2.71	1.82	13.6	63.1	268	M1
	171.5	0.57(7)	0.064	0.25	0.87	0.49	2.75	11.8	48.8	M1
	343.9	0.14(3)	0.011	0.034	0.097	0.074	0.27	0.84	2.56	M1
	436.7		0.006	0.018	0.048	0.040	0.13	0.36	0.96	M1
	630.5	0.27(3)	0.003	0.008	0.018	0.017	0.047	0.11	0.25	M4
^{154}Yb	133.2	0.11(4)	0.13	0.51	1.69	1.19	7.71	34.0	14	E1
^{154}Lu	96.6	1.3(3)	0.31	1.09	2.94	3.24	26.2	109	394	E2

[a] F. Rosel, H.M. Fries, K. Alder, and H.C. Pauli, At. Data and Nucl. Data Tables 21 ,91(1978).

[b] α_{tot}(expt)

Table 6. Comparison of experimental and calculated proton final state branches.

Precursor	J^π	Energy	Branching Intensity (%)				
(Adopted J^π)	Daughter	(kev)	Exp.	$1/2^+$	$3/2^+$	$5/2^+$	$7/2^+$
^{119}Ba	0^+	0	71(10)	60	46	21	-
$(1/2^+)$	2^+	337	29(5)	33	45	60	-
	4^+	810	1(1)	1	1	9	-
^{123}Ce	0^+	0	23(6)	-	37	14	9
$(5/2^+)$	2^+	197	66(6)	-	55	66	54
	4^+	570	9(3)	-	3	14	32
	6^+	1083	2(1)	-	-	-	1
^{125}Ce	0^+	0	36(4)	-	49	20	14
$(5/2^+)$	2^+	230	53(4)	-	50	72	65
	4^+	651	9(3)	-	1	8	21
	6^+	1228	1(1)	-	-	-	-
^{127}Nd	0^+	0	60(15)	50	37	14	-
$(1/2^+)$	2^+	170	35(13)	48	60	70	-
	4^+	520	5(5)	2	3	16	-
^{129}Nd	0^+	0	23(7)	-	44	17	12
$(5/2^+)$	2^+	207	68(7)	-	54	71	61
	4^+	607	9(3)		2	12	27
^{131}Nd	0^+	0	32(7)	-	57	26	20
$(5/2^+)$	2^+	254	67(7)	-	41	68	67
	4^+	710	1(1)		1	4	11
^{131}Sm	0^+	0	41(15)	47	35	13	7
$(5/2^+)$	2^+	158	36(15)	51	61	68	52
	4^+	483	21(8)	2	4	19	39
	6^+	938	3(3)	-	-	1	2
^{133}Sm	0^+	0	35(9)	56	43	18	-
$(3/2^+)$	2^+	213	63(9)	43	54	70	-
	4^+	611	1(1)	1	3	12	-
^{135}Sm	0^+	0	42(13)	64	52	24	-
$(5/2^+)$	2^+	294	41(14)	31	41	61	-
	2^+	754	10(6)	4	6	8	-
	4^+	789	7(5)		1	5	-

Table 7. Experimental and calculated β-delayed proton branches from ^{153}Yb to levels in ^{152}Er.

Levels in ^{152}Er		Final State Branches (%)			
J^{π}	Energy (keV)	Experiment	Gross Theory $7/2^-$	QRPA $7/2^-$	Constant $7/2^-$
0^+	0	57(17)	50	66	49
2^+	808	40(12)	44	32	45
4^+	1481	3(3)	4	2	4

Table 8. Isotopes Studied at OASIS

Isotope	$t_{1/2}$(s)	Decay
^{119}Ba	6.0(3)	βp
^{120}La	2.8(4)	βp
^{122}La	8.7(7)	βp
^{123}Ce	3.8(2)	βp
^{125}Ce	9.8(8)	βγp
^{124}Pr	1.2(2)	βp
^{126}Pr	3.2(6)	βγp
^{128}Pr	4(1)	βp
^{127}Nd	1.8(4)	βp
^{129}Nd	4.9(3)	βp
^{131}Nd	25(5)	βp
^{130}Pm	2(1)	βp
^{132}Pm	5(1)	βγp
^{134}Pm(2$^+$)	~3-20	βγ
^{134}Pm(5$^+$)	22.6(5)	βγ
^{135}Pm(5/2$^+$)	~45	βγ
^{135}Pm(11/2$^-$)	49(3)	βγ
^{136}Pm(2$^+$)	~30-150	βγ
^{136}Pm(5$^+$)	a	βγ
^{142}Pm	a	βγ
^{131}Sm	1.2(2)	βp
^{133}Sm	2.8(5)	βp
^{134}Sm	10(3)	βγ
^{135}Sm	10.3(5)	βγp
^{136}Sm	a	βγ
^{141}Sm	a	βγ
^{142}Sm	a	β
^{134}Eu	0.5(2)	βp
^{135}Eu	1.5(2)	βγ
^{136}Eu(3$^+$)	3.7(3)	βγp
^{136}Eu(6$^+$,7$^+$)	~3	βγp
^{140}Eu(1$^+$)	1.51(2)	βγ
^{140}Eu(5$^-$)	0.125(2)	IT
^{141}Eu(11/2$^-$)	3.3(3)	βγ
^{141}Eu(5/2$^+$)	a	βγ
^{142}Eu	2.34(12)	βγ
^{137}Gd	7(3)	βp
^{139}Gd	5(1)	βp
^{140}Gd	15.8(4)	βγp
^{141}Gd(11/2$^-$)	24.5(5)	βγ
^{141}Gd(1/2$^+$)	14(4)	βγp
^{142}Gd	70.2(6)	βγ
^{140}Tb	2.4(2)	βγp
^{141}Tb	3.5(2)	βγ
^{142}Tb(1$^+$)	0.597(17)	βγp
^{142}Tb(5$^-$)	0.303(17)	IT
^{144}Tb(1$^+$)	a	βγ
^{144}Tb(6$^-$)	4.1(1)	βγ
^{145}Tb	a	βγ
^{141}Dy	0.9(2)	βγp
^{142}Dy	2.3(3)	βγp
^{143}Dy	3.1(3)	βp
^{144}Dy	9.1(5)	βγp
^{145}Dy	8(1)	βγp
^{147}Dy(11/2$^-$)	a	βγ
^{147}Dy(1/2$^+$)	a	βγp
^{149}Dy	a	βγ
^{168}Dy	a	βγ
^{169}Dy	55(3)	βγ
^{144}Ho	0.7(2)	βp
^{145}Ho	2.4(1)	βγ
^{146}Ho	3.1(5)	βγp
^{148}Ho	9.7(3)	βγp
^{149}Ho(11/2$^-$)	21.4(3)	βγ
^{149}Ho(1/2$^+$)	54(2)	βγ
^{169}Ho	a	βγ
^{171}Ho	54(3)	βγ
^{145}Er	0.9(3)	βp
^{147}Er	2.6(2)	βp
^{148}Er	4.4(2)	βγp
^{149}Er(11/2$^-$)	8.9(2)	βγp
^{149}Er(1/2$^+$)	4(2)	βγp
^{151}Er	a	βγ
^{174}Er	198(12)	βγ
^{149}Tm	0.9(2)	βγp
^{150}Tm	2.2(2)	βγp
^{151}Tm	a	βγ
^{153}Tm(11/2$^-$)	1.7(2)	α,βγ
^{153}Tm(1/2$^+$)	~0.5-2.5	α,βγ
^{174}Tm	a	βγ
^{151}Yb(11/2$^-$)	1.6(1)	βp
^{151}Yb(1/2$^+$)	1.6(1)	βγp
^{153}Yb	3.9(1)	βγp
^{154}Yb	0.42(5)	α,βγ
^{155}Yb	1.75(5)	α,βγ
^{152}Lu	0.7(1)	βp
^{153}Lu	0.9(2)	βγ
^{154}Lu	1.2(1)	βγpα
^{155}Lu(3/2$^+$,1/2$^+$)	0.140(14)	α
^{155}Lu(11/2$^-$)	0.066(7)	α
^{157}Lu(1/2$^+$,3/2$^+$)	5.7(6)	α,βγ
^{157}Lu(11/2$^-$)	4.8(5)	α,βγ
^{166}Lu(0$^-$)	a	βγ
^{166}Lu(3$^-$)	a	βγ
^{166}Lu(6$^-$)	a	βγ
^{168}Lu(3$^+$)	a	βγ
^{168}Lu(6$^-$)	a	βγ
^{169}Lu(1/2$^-$)	a	IT
^{171}Lu(1/2$^-$)	a	IT
^{172}Lu(1$^-$)	a	IT

[a] Half-life not determined in these experiments

TABLE 9. Systematics of N=81 Beta Decays

	Dominant core configuration[a]					
	$2^+,3^-$		$4^+,5^-,6^+,7^-$		$(\nu h_{9/2})$	
Transition	E_x [b]	log*ft*	E_x [b]	log*ft*	E_x [b]	log*ft*
$^{149}Er^m \rightarrow {}^{149}Ho$	1523	5.2	2498	5.0	4530	4.4
$^{149}Er^g \rightarrow {}^{149}Ho$	1797	>4.2			4700	4.2
$^{148}Ho^{g+m} \rightarrow {}^{148}Dy$	1682	~5.5	2653	~4.9	4300	<5.1
$^{147}Dy^m \rightarrow {}^{147}Tb$	1482	5.2	2260	4.9	4800	3.9
$^{147}Dy^g \rightarrow {}^{147}Tb$	1763	5.0			4100	~3.7
$^{146}Tb^{g+m} \rightarrow {}^{146}Gd$	1971	~5.4	2841	4.6	4730	4.5
$^{145}Gd^g \rightarrow {}^{145}Eu$	1819	5.4			4500	4.4
$^{144}Eu^{g+m} \rightarrow {}^{144}Sm$	1660	4.9	2450	5.1		

[a]Core configuration that is coupled to the $\pi s_{1/2}$ or the $\pi h_{11/2}$ odd proton in the daughter nucleus.

[b]Intensity weighted average excitation energy of the core-coupled configurations populated by beta decay.

Table 10. Comparison of experimental and calculated B(E2) values at N≈82.

		B(E2) e^2fm^4	
Transition	n	Experiment	Shell Model[a]
^{148}Dy($10^+ \rightarrow 8^+$)	2	44(3)	≡44
^{149}Ho($27/2^- \rightarrow 23/2^-$)	3	88(6)	92
^{150}Er($10^+ \rightarrow 8^+$)	4	11.4(14)	10.8
^{150}Er($8^+ \rightarrow 6^+$)	4	~37	27.3
^{151}Tm($27/2^- \rightarrow 23/2^-$)	5	12.1(7)	9.2
^{152}Yb($10^+ \rightarrow 8^+$)	6	0.9(1)	0
^{153}Lu($27/2^- \rightarrow 23/2^-$)	7	0.45(9)	9[b]
^{154}Hf($10^+ \rightarrow 8^+$)	8	2.9(14)	11[b]

[a] R.D. Lawson, Z. Phys. A303, 51 (1981).

[b] Estimated values assuming $(6\text{-}n)^2$ scaling.

FIGURE CAPTIONS

Figure 1. OASIS experimental apparatus. The exploded drawings circled on the left show the detectors (upper) and ion source (lower) in greater detail.

Figure 2. Fit to Q_{EC}-B_p for $^{149}Er^g$ decay to levels associated with structured proton decay. The χ^2/f from comparison of the experimental $\beta^+/(\beta^+ + EC)$ values with the theoretical ratios is plotted on the ordinate for various Q_{EC}-B_p values indicated on the abscissa. The uncertainty is chosen to encompass all values with $\chi^2/f<1$.

Figure 3. Decay scheme for $^{142}Tb^m$.

Figure 4. $^{142}Tb^m$ coincidence data.

Figure 5. Spectrum of β-delayed protons from ^{149}Er decay.

Figure 6. Decay scheme for ^{141}Tb.

Figure 7. Proton (a) and neutron (b) single-particle level energies for ^{141}Dy as a function of spheroidal deformation, based on the Nilsson model with a folded Yukawa potential. In the calculations, the range of the Yukawa function was $a_p=a_n=0.80$ fm and the proton spin-orbit interaction strengths were $\lambda_p=31.52$ and $\lambda_n=34.14$, respectively. A constant $\varepsilon_4=0.04$ was assumed.

Figure 8. Proton and Neutron single-particle shell model orbitals for rare earth nuclei.

Figure 9. Log*ft* systematics for $0^+ \rightarrow 1^+$ transitions.

Figure 10. Single-particle shell model predictions for log*ft* values of $\pi d_{5/2} \rightarrow \nu d_{3/2}$ and $\pi h_{11/2} \rightarrow \pi h_{9/2}$ spin-flip transitions as a function of *n* particles in the valence proton orbitals.

Figure 11. Log*ft* systematics for $5/2^+ \rightarrow 3/2^+$ transitions.

Figure 12. Log*ft* systematics for $11/2^- \rightarrow 9/2^-$ transitions.

Figure 13. Log*ft* systematics for $1^+ \rightarrow 0^+$ transitions.

Figure 14. Log*ft* systematics for $9^+ \rightarrow 8^+$ transitions.

Figure 15. Systematics of Weisskopf-reduced B(M4) γ-ray transition probabilities.

Figure 16. Systematics of Weisskopf-reduced B(E3) γ-ray transition probabilities.

Figure 17. Systematics of Weisskopf-reduced B(M2) γ-ray transition probabilities.

Fig. 1

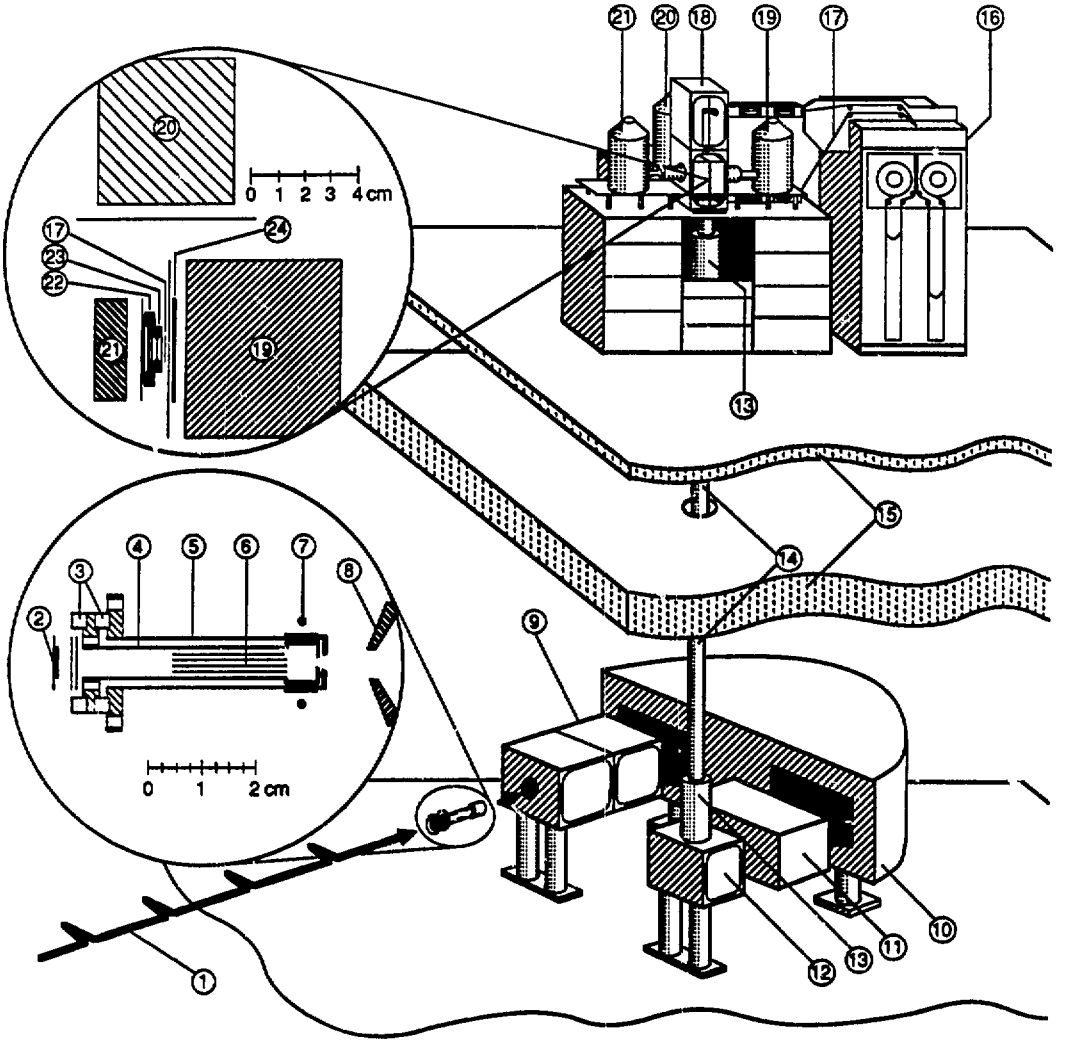

1. SuperHILAC BEAM
2. TARGET
3. INSULATORS (BeO)
4. ION SOURCE ANODE (Ta)
5. ION SOURCE CATHODE (Ta)
6. CAPILLARY TUBES (Ta)
7. EB FILAMENT (Ta)
8. EXTRACTION ELECTRODE
9. EXTRACTION AND FOCUSING
10. ANALYZING MAGNET
11. FOCAL PLANE DETECTOR BOX
12. ELECTROSTATIC MIRROR
13. ELECTROSTATIC QUADRUPOLE
14. TRANSFER LINE
15. CONCRETE SHIELDING
16. TAPE DRIVE (IBM 729)
17. MAGNETIC TAPE
18. DETECTOR BOX
19. N-TYPE Ge DETECTOR (52%)
20. N-TYPE Ge DETECTOR (24%)
21. HPGe DETECTOR
22. 718 μm Si DETECTOR
23. 10.4 μm Si DETECTOR
24. 1mm PILOT F SCINTILLATOR

Fig. 2

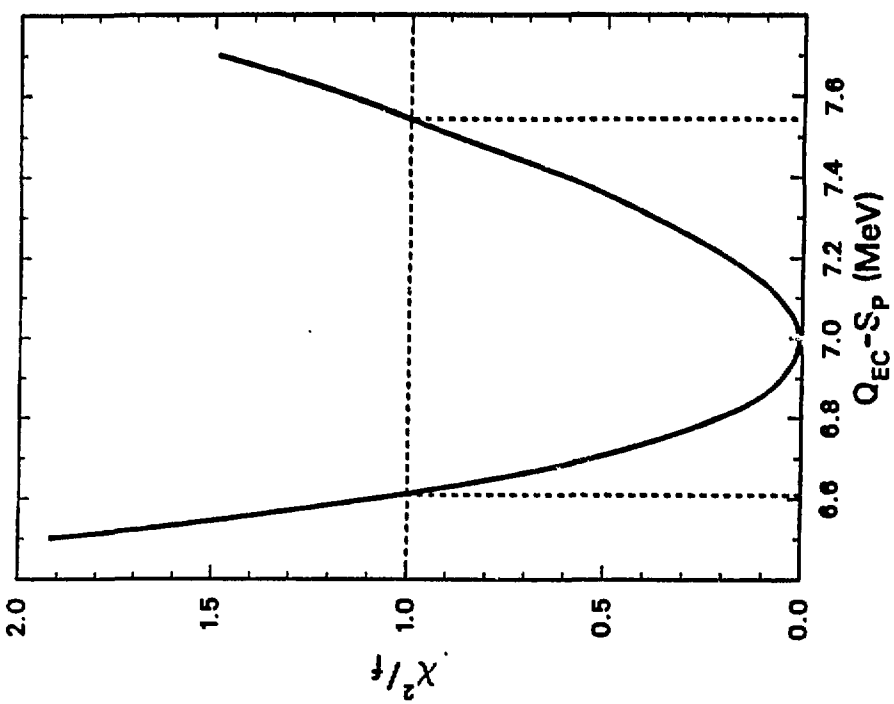

Fig. 3

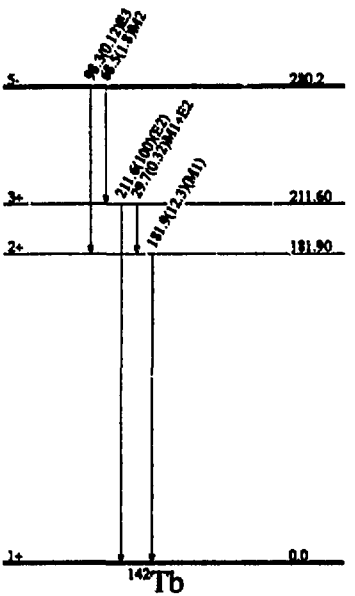

Fig. 4

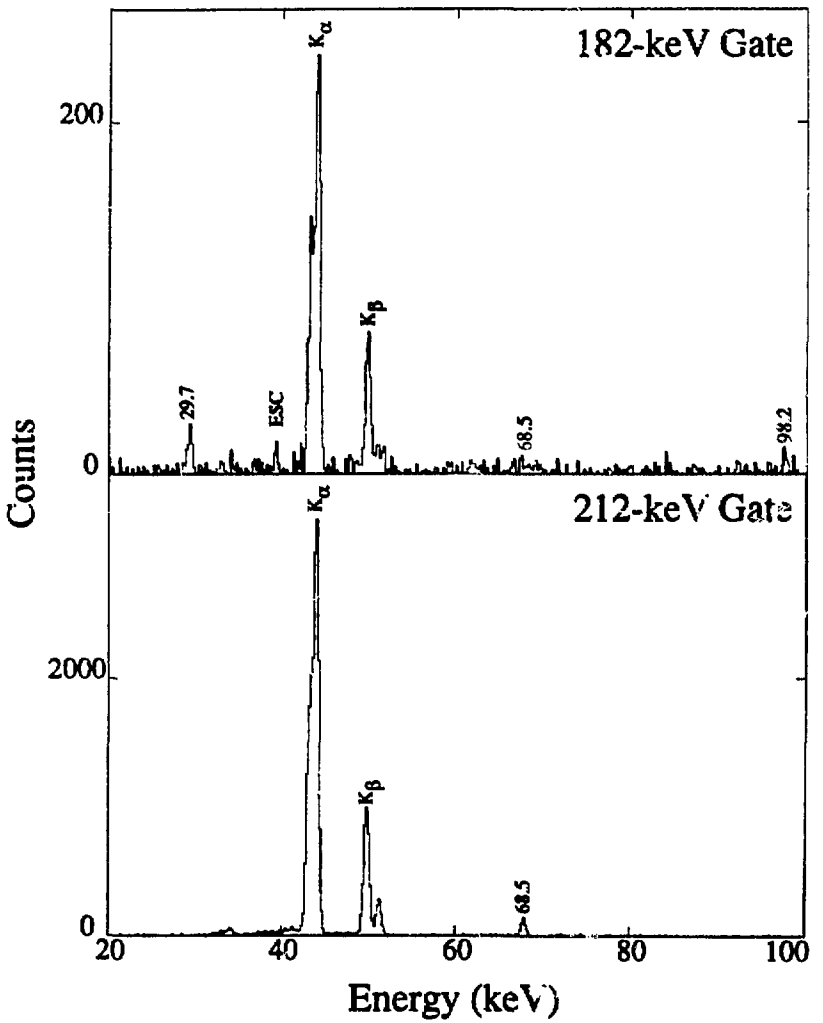
182-keV Gate
212-keV Gate
Counts
Energy (keV)
K_α
K_β
ESC
29.7
68.5
98.2
200
0
2000
20
40
60
80
100

Fig. 5

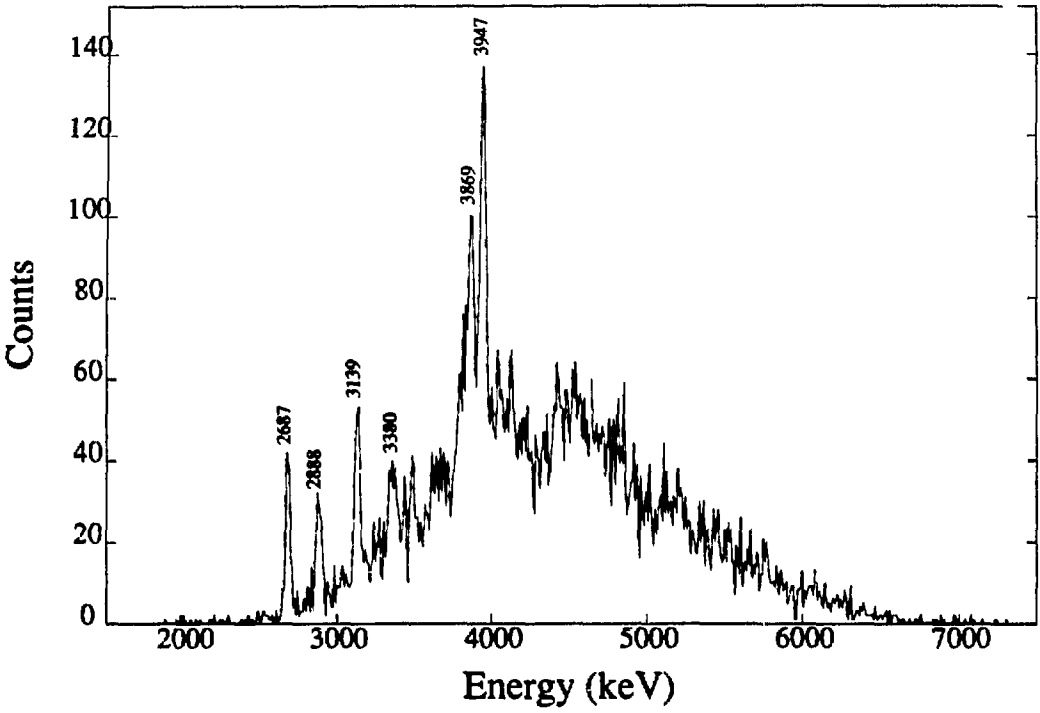
Counts
Energy (keV)
2687
2888
3139
3380
3869
3947
0
20
40
60
80
100
120
140
2000
3000
4000
5000
6000
7000

Fig. 6

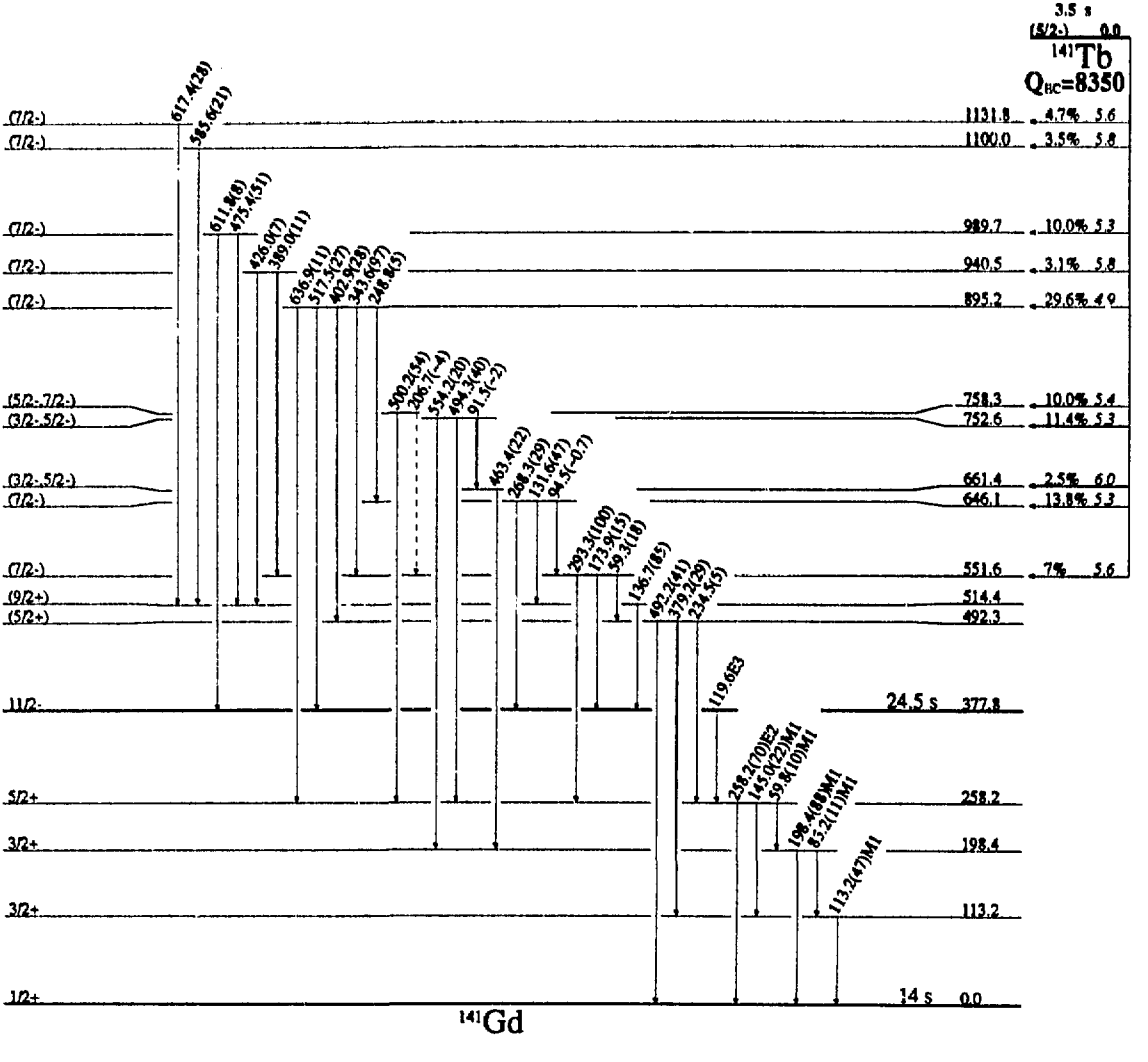
3.5 s
(5/2-) 0.0
141Tb
QEC=8350
(7/2-) 1131.8 4.7% 5.6
(7/2-) 1100.0 3.5% 5.8
(7/2-) 989.7 10.0% 5.3
(7/2-) 940.5 3.1% 5.8
(7/2-) 895.2 29.6% 4.9
(5/2-,7/2-) 758.3 10.0% 5.4
(3/2-,5/2-) 752.6 11.4% 5.3
(3/2-,5/2-) 661.4 2.5% 6.0
(7/2-) 646.1 13.8% 5.3
(7/2-) 551.6 7% 5.6
(9/2+) 514.4
(5/2+) 492.3
11/2- 24.5 s 377.8
5/2+ 258.2
3/2+ 198.4
3/2+ 113.2
1/2+ 14 s 0.0
141Gd
617.4(28)
585.6(21)
611.8(8)
475.4(31)
426.0(7)
389.0(11)
636.9(11)
517.5(27)
402.8(28)
343.8(67)
248.8(5)
500.2(54)
206.7(-4)
554.2(20)
494.3(60)
91.5(-2)
463.4(22)
268.3(29)
131.6(47)
94.5(-0.7)
293.3(100)
173.9(15)
59.3(18)
136.7(85)
492.2(41)
379.2(29)
234.5(5)
119.6E3
258.2(70)E2
145.0(22)M1
59.8(10)M1
198.4(88)M1
85.2(11)M1
113.2(47)M1

Fig. 7

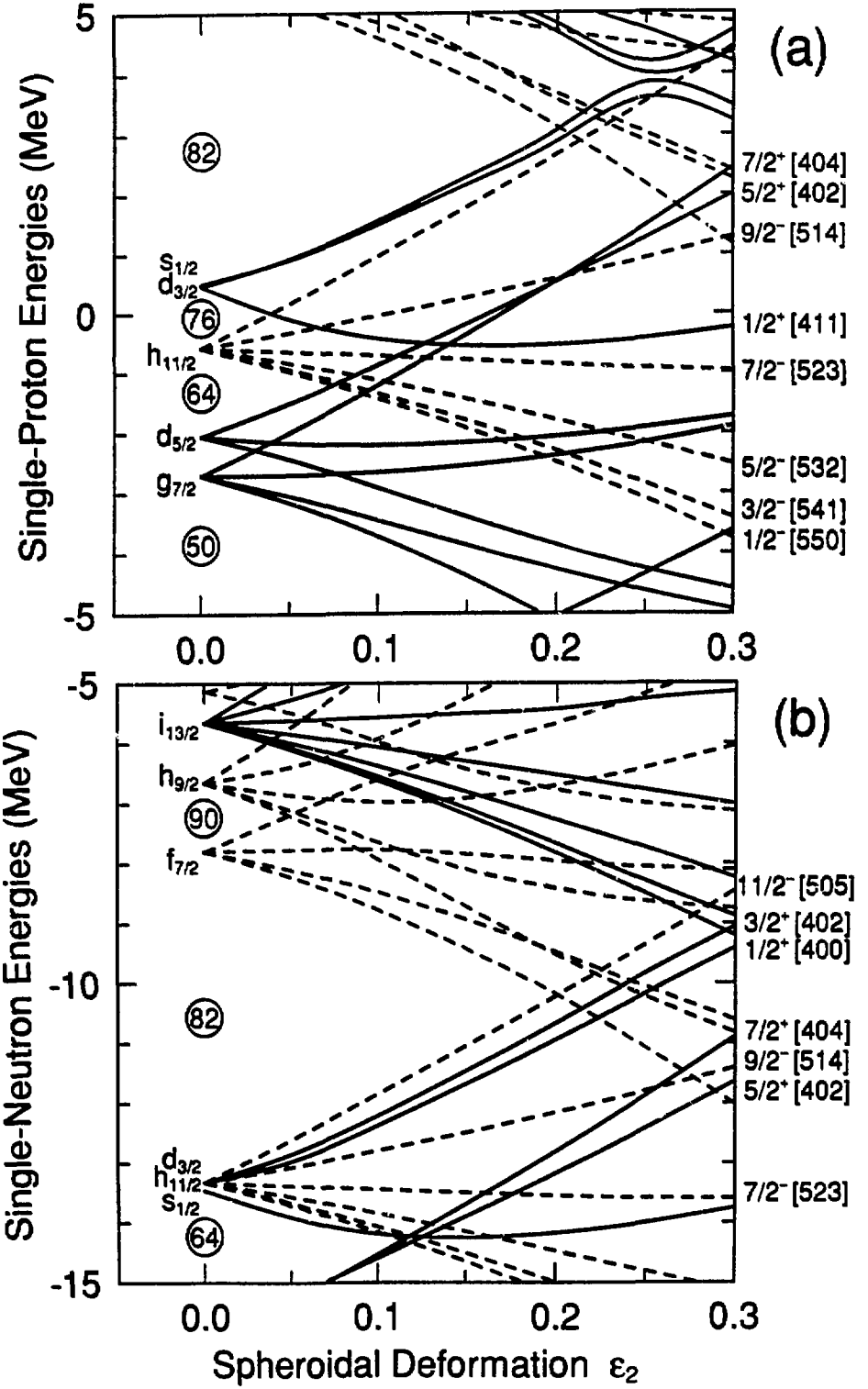
(a)
Single-Proton Energies (MeV)
5
0
-5
0.0
0.1
0.2
0.3
82
76
64
50
$s_{1/2}$
$d_{3/2}$
$h_{11/2}$
$d_{5/2}$
$g_{7/2}$
7/2⁺ [404]
5/2⁺ [402]
9/2⁻ [514]
1/2⁺ [411]
7/2⁻ [523]
5/2⁻ [532]
3/2⁻ [541]
1/2⁻ [550]
(b)
Single-Neutron Energies (MeV)
-5
-10
-15
0.0
0.1
0.2
0.3
Spheroidal Deformation ε_2
90
82
64
$i_{13/2}$
$h_{9/2}$
$f_{7/2}$
$d_{3/2}$
$h_{11/2}$
$s_{1/2}$
11/2⁻ [505]
3/2⁺ [402]
1/2⁺ [400]
7/2⁺ [404]
9/2⁻ [514]
5/2⁺ [402]
7/2⁻ [523]

Fig. 8

SHELL MODEL STATES NEAR Z=64 AND N=82

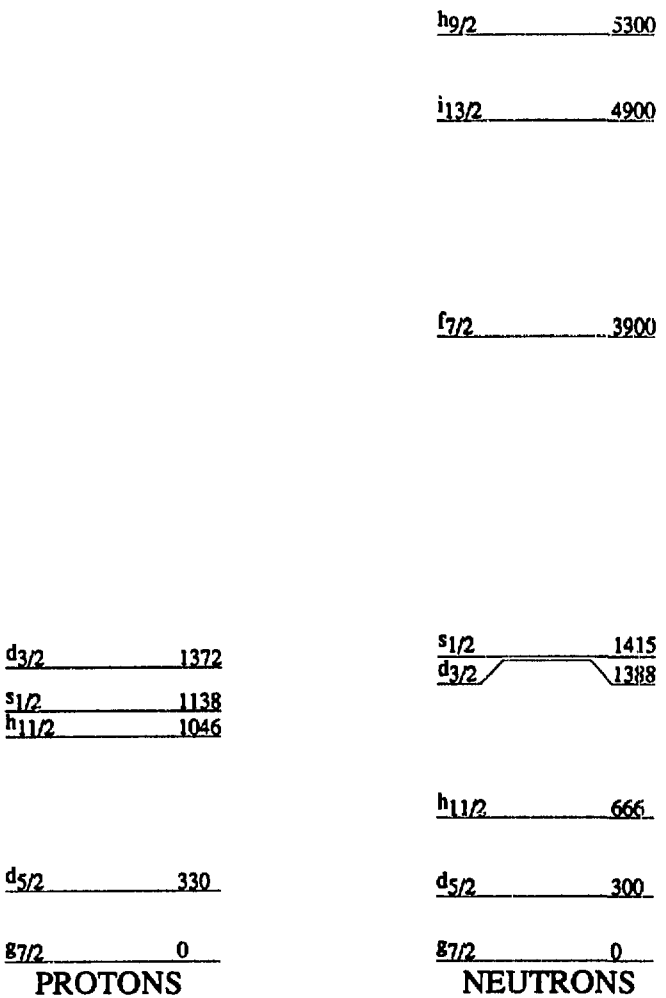

Fig. 9

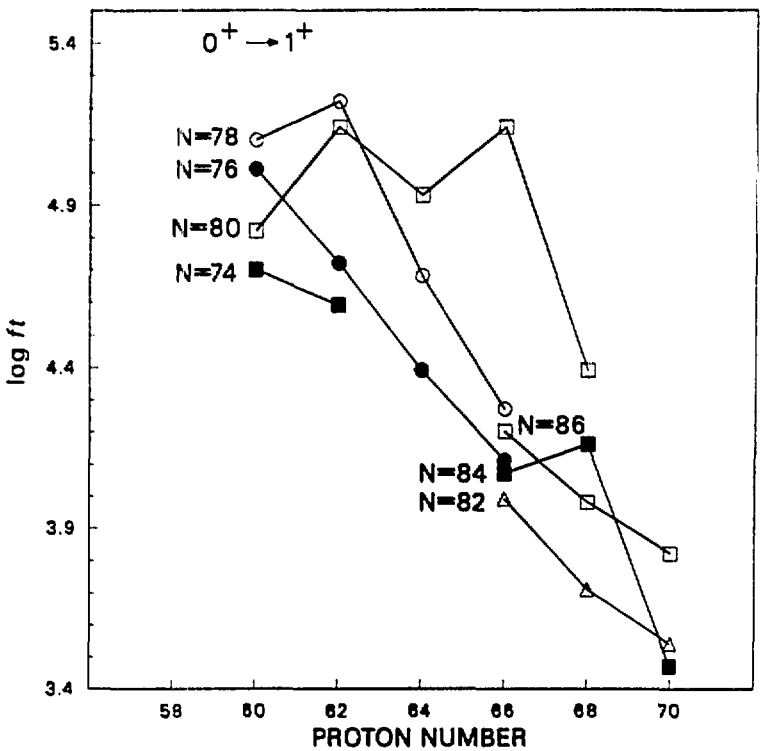
$0^+ \rightarrow 1^+$
N=78
N=76
N=80
N=74
N=86
N=84
N=82
log ft
5.4
4.9
4.4
3.9
3.4
58
60
62
64
66
68
70
PROTON NUMBER

Fig. 10

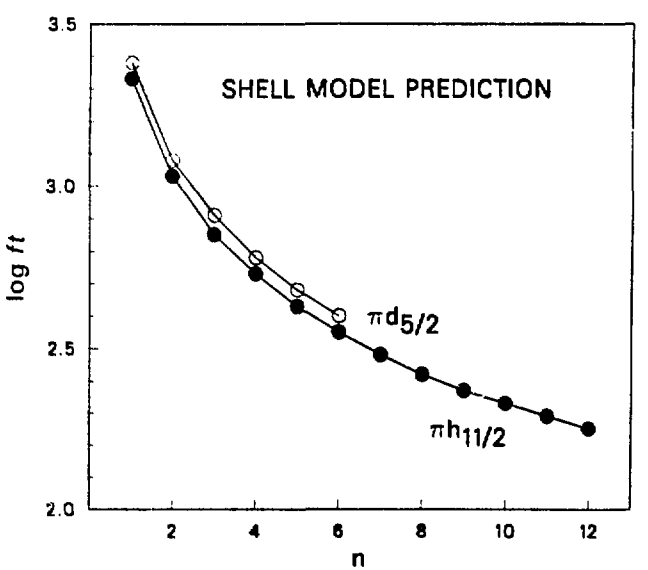
SHELL MODEL PREDICTION
πd5/2
πh11/2
log ft
n
3.5
3.0
2.5
2.0
2
4
6
8
10
12

Fig. 11

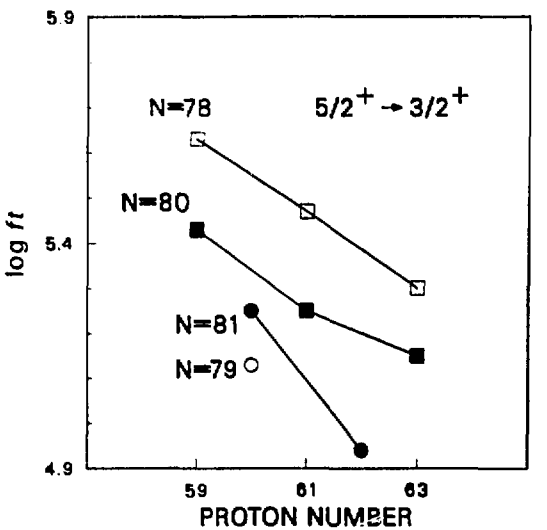

Fig. 12

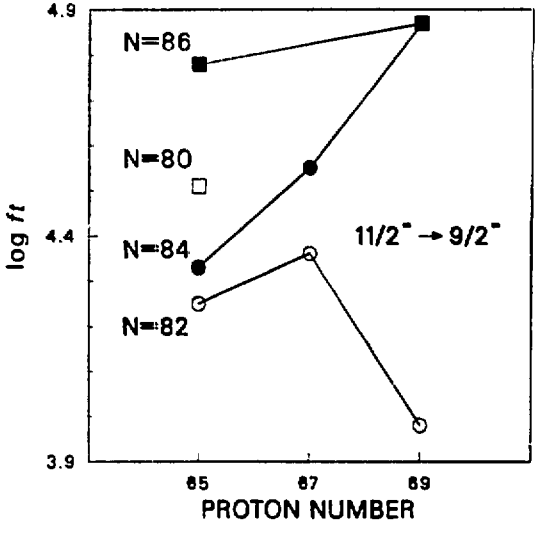

Fig. 13

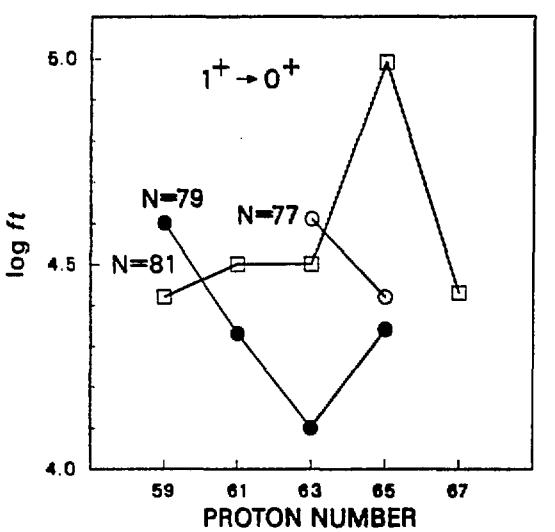

Fig. 14

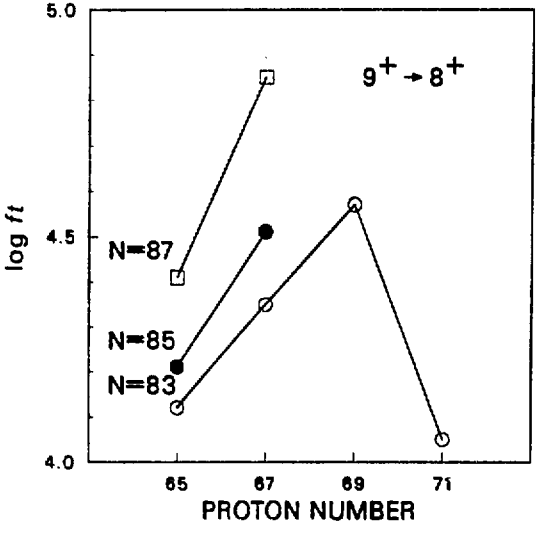

Fig. 15

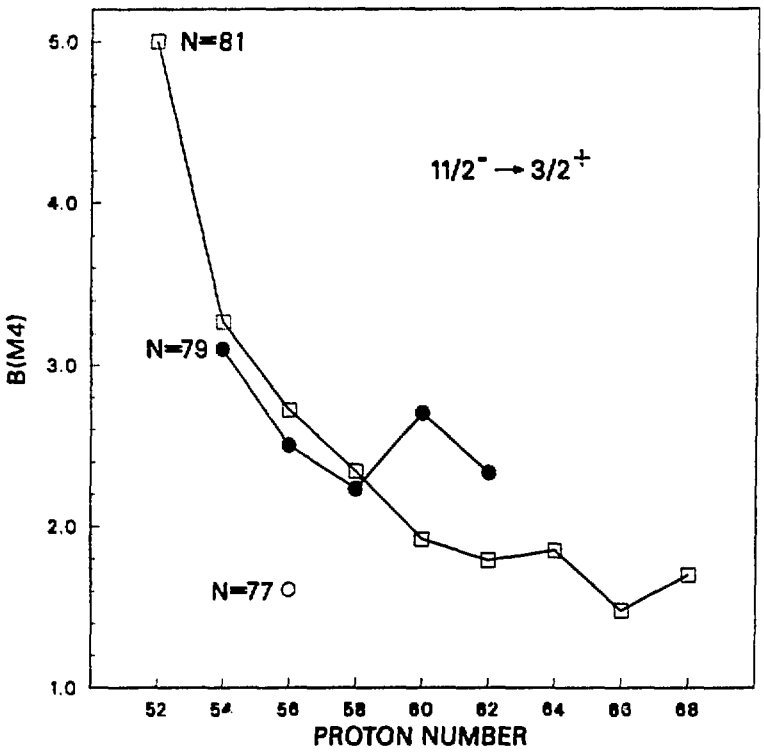
N=81
11/2⁻ → 3/2⁺
N=79
N=77
B(M4)
5.0
4.0
3.0
2.0
1.0
52
54
56
58
60
62
64
66
68
PROTON NUMBER

Fig. 16

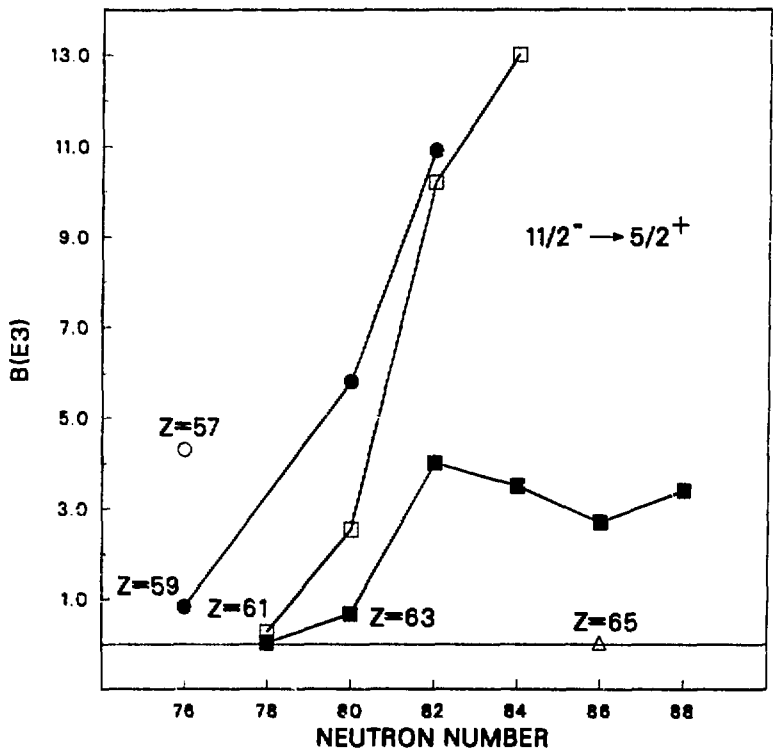
13.0
11.0
9.0
7.0
5.0
3.0
1.0
B(E3)
11/2⁻ → 5/2⁺
Z=57
Z=59
Z=61
Z=63
Z=65
76
78
80
82
84
86
88
NEUTRON NUMBER

Fig. 17

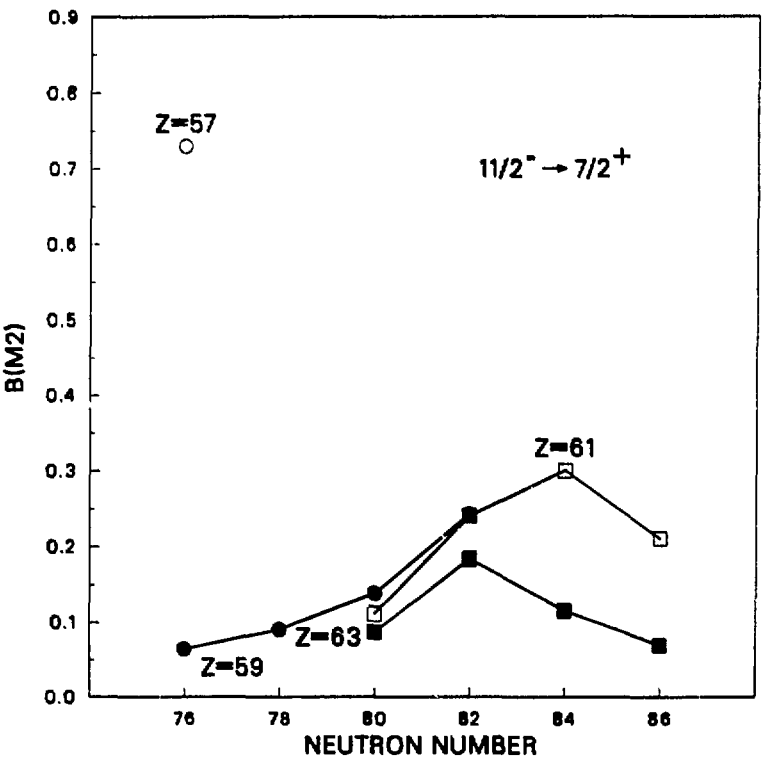
0.9
0.8
0.7
0.6
0.5
0.4
0.3
0.2
0.1
0.0
B(M2)
Z=57
11/2⁻ → 7/2⁺
Z=61
Z=63
Z=59
76
78
80
82
84
86
NEUTRON NUMBER